Anomalous exchange interactions between RE^{+3} and Mn^{+3} moments in multiferroic h-$REMnO_3$

N. J. Laurita,[1] Yi Luo,[1] Rongwei Hu,[2] Meixia Wu,[2] S. W. Cheong,[2] O. Tchernyshyov,[1] and N. P. Armitage[1]

[1] *The Institute for Quantum Matter, Department of Physics and Astronomy, The Johns Hopkins University, Baltimore, MD 21218, USA*

[2] *Rutgers Center For Emergent Materials, Department of Physics and Astronomy, Rutgers University, Piscataway, NJ, 08854, USA*

(Dated: July 27, 2022)

The multiferroic hexagonal rare-earth manganites h-$REMnO_3$ display a diverse array of magnetic phenomena, as many contain both rare-earth and Mn magnetic moments which interact in a low symmetry crystal structure. Of these materials h-$HoMnO_3$ (HMO) possesses the largest rare-earth magnetic moment and is therefore ideal for investigating magnetic exchange in hexagonal manganites. In this work, time-domain THz spectroscopy experiments uncover evidence for exceptionally strong and unconventional Ho-Mn spin interactions in HMO through careful examination of an antiferromagnetic resonance (AFR) of the Mn sublattice. Experiments reveal the AFR to split *asymmetrically* in magnetic field with substantially different g-factors for the high and low energy branches of this excitation. The temperature dependence reveals this asymmetry to be related to the Ho sublattice magnetization. Furthermore, we uncover a drastic renormalization of the g-factors of the Mn AFR at the Ho spin ordering temperature, confirming strong Ho-Mn coupling. Theoretical calculations demonstrate these results are not explained by conventional exchange mechanisms and therefore suggest a new Ho-Mn spin interaction in HMO. Our results provide a paradigm for the optical study of such spin interactions in other hexagonal manganites.

arXiv:1706.04141v1 [cond-mat.str-el] 13 Jun 2017

Interactions between localized spins in magnetic insulators are heavily influenced by the symmetry of the crystal structure in which they are embedded. Accordingly, crystals with particularly low symmetry permit spins to interact through unconventional exchange mechanisms, sometimes resulting in novel phenomena or new states of matter. The hexagonal rare-earth manganites h-$REMnO_3$ are prime examples of materials whose low symmetry results in a plethora of remarkable physical behavior [1]. These non-centrosymmetric insulators are a robust class of multiferroics as well as exceptionally strong magnetoelectrics [2]. Magnetism in these systems is hallmarked by both rare-earth and manganese magnetic moments, which are contained to lie in orthogonal directions due to strong crystalline anisotropy [3]. Interactions between these moments have been a topic of intense investigation [3–7] as such couplings are thought to drive magnetic transitions [8] as well as mediate magnetoelectric phenomena in these materials [9, 10]. However, the exchange mechanism between RE-Mn spins has remained elusive, as their orthogonality suggests a less conventional spin interaction than Heisenberg exchange in the equilibrium spin configuration.

Of these materials, h-$HoMnO_3$ (HMO) possesses the largest effective rare-earth magnetic moment and is thus ideal for studying magnetic exchange in these systems [2, 11–14]. The hexagonal crystal structure of HMO consists of alternating layers of corner sharing MnO_5 bipyramids and Ho ions which are stacked along the c axis. At the ferroelectric transition, $T_c = 875$K, the MnO_5 bipyramids buckle [15–17] reducing the symmetry to the non-centrosymmetric polar space group $P6_3cm$. In this phase the Ho ions occupy the symmetry distinct 2a and 4b positions of the crystal lattice. The S_{Mn}=2 spins form a two-dimensional frustrated triangular lattice which order at $T_N \approx 75$K, in a 120 degree structure with symmetry $P6_3^{'}c^{'}m$ [18–23]. Two additional zero field Mn sublattice transitions occur at $T_{SR} \approx 40$K ($P6_3^{'}cm^{'}$) and at $T_{Ho} \approx 5$K ($P6_3cm$), in which the Mn spins rotate by 90 degrees within the basal plane. The ordering of the Ho sublattices is less understood [3, 18–25], however it is expected that the S_{Ho}=2 spins order antiferromagnetically along the c axis due to uniaxial anisotropy [3], with experimental evidence suggesting that magnetization of at least one of the Ho sublattices onsets near T_{SR} [3, 25]. Regardless, it is agreed that long range order exists within at least one of the Ho sublattices below T_{Ho}.

Interactions between RE and Mn moments in hexagonal manganites can be probed by examining the spin excitations of the Mn sublattice. A minimal spin Hamiltonian of the Mn triangular sublattice is given by:

$$H = J \sum_{<ij>} \mathbf{S}_i \cdot \mathbf{S}_j + \Delta \sum_i (S_i^z)^2 - g\mu_B \mathbf{B} \cdot \sum_i \mathbf{S}_i, \quad (1)$$

where J is the Heisenberg exchange, Δ is the planar anisotropy, $\mathbf{B}$ is the applied magnetic field along the c axis, $g = 2$ is the Mn g-factor, and the sum is over neighboring pairs [21, 26]. The ground state of the Mn sublattice is a 120° ordered AF. In the $\vec{k} \to 0$ limit (applicable to our optical measurements) the low energy spectrum consists of a Goldstone mode as well as a gapped antiferromagnetic resonance (AFR) [26]. In the weak field limit, valid for fields $H < S_{Mn}J \approx 40$T in HMO, the energies

of the AFR are given by:

$$\hbar\omega_{\pm}(B) = \hbar\omega(0) \pm g_{\text{eff}}\mu_B B, \quad \hbar\omega(0) = 3S\sqrt{J\Delta}, \quad (2)$$

revealing two modes which split symmetrically in field with $g_{\text{eff}} = \frac{g}{2+4\Delta/9J}$ [27]. With exchange and anisotropy found to be $J = 2.44$ meV and $\Delta = 0.38$ meV respectively in HMO [21], one expects $g_{\text{eff}} = 0.97$ from Equation 2. Note that even in the limit of small anisotropy, g_{eff} is approximately half of that of the expected bare ionic value. This is a particular feature of the 120° ordered AF and arises due to the fact that low symmetries of the ordered state mean that z angular momentum is not a good quantum number. With increasing Δ even smaller values are expected. However, in actuality much larger g-factors are observed at low temperatures [6] in both HMO and other hexagonal manganites with rare-earth magnetism [27]. This has been explained by introducing an additional Heisenberg exchange interaction which ferromagnetically couples RE spins to the finite S_z of the Mn AFR modes into Equation 7 [6]. However, such a coupling is expected to vanish in the ground state due to the orthogonality of spins, thus leaving the dominant equilibrium RE-Mn spin interaction unresolved.

In this letter, we present a systematic study of the low energy optical response of HMO via high resolution time-domain terahertz spectroscopy (TDTS). We demonstrate that the Mn AFR possesses distinct selection rules to circularly polarized light, which allows our experiments to resolve the field dependent splitting of the AFR in small magnetic fields with high precision. In addition to observing g-factors much larger than the Mn only value, the AFR is also found to unexpectedly split *asymmetrically*. We demonstrate that this asymmetry results from RE-Mn interactions by careful study of the temperature dependence of the g-factors, which are found to be greatly enhanced at T_{Ho}, the temperature at which the Ho spins are known to order. We interpret these observations as the result of an additional RE-Mn spin interaction, which the data coupled with our theoretical investigations allows us to conclude does not result from conventional Dzyaloshinkii-Moriya [28, 29] interactions alone, suggesting the presence of a novel spin interaction in HMO. The potential for such spin interactions in other hexagonal manganites is discussed.

Single crystals of HMO were grown via optical floating zone method. Two samples with the orientations of [-1,1,0] (d = 670 μm) and [0,0,1] (d = 590 μm) normal to the sample surface were measured in this study. TDTS transmission experiments were performed using a home built spectrometer [30] with applied magnetic fields up to 6T in Faraday geometry ($\vec{k}_{\text{THz}} \parallel \vec{H}_{\text{dc}}$). The fundamental quantity measured in a TDTS experiment is the complex transmission spectrum, found by taking the ratio of the transmitted electric field through a sample to that of an aperture of identical size. Via a coupling of the

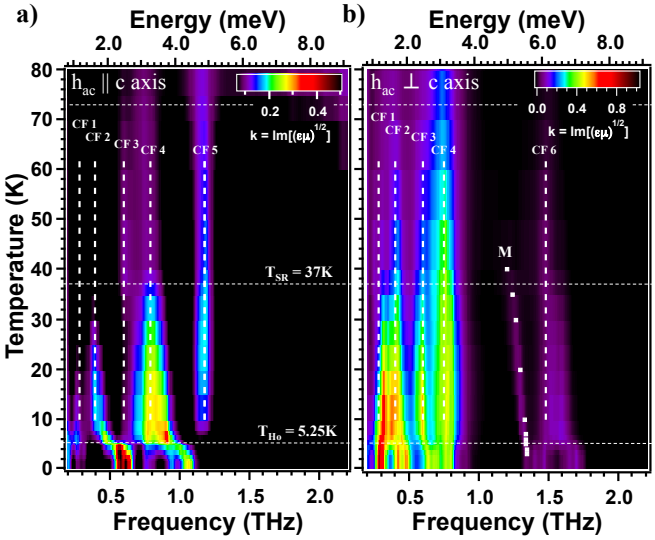

FIG. 1: Image plots of the imaginary part of the index of refraction as a function of temperature and frequency for the orientations (a) $\vec{h}_{\text{ac}} \parallel$ c and (b) $\vec{h}_{\text{ac}} \perp$ c respectively. Horizontal dashed lines denote the three zero field transition temperatures while vertical dashed label the more prominent Ho crystal field excitations identified at temperatures $T \geq T_{\text{Ho}}$. The excitation labeled "M" is the AFR of the Mn sublattice. White circles denote the AFR resonant frequency found by fitting the spectra as described in the text.

THz fields to both electric and magnetic dipole transitions of the sample, TDTS accesses the sample's electromagnetic response with exceptional resolution from 0.2 - 2 THz. The hexagonal symmetry of HMO along with the $\mathcal{T}$ symmetry breaking under applied field constrains the linear response transmission matrix such that it can be only diagonalized by a circular basis transformation, revealing circularly polarized light to be the natural eigenpolarizations for this system [31]. TDTS measurements performed in this study utilized a rotating polarizer technique, which allows for measurement of the sample's response to two polarization directions simultaneously and conversion to the circular basis [32].

Figure 1 displays the full temperature dependence of the far-infrared optical response of HMO. Shown are image plots of the imaginary, or dissipative, part of the complex index of refraction, $\tilde{n} = n + ik$, for the orientations (a) $\vec{h}_{\text{ac}} \parallel$ c and (b) $\vec{h}_{\text{ac}} \perp$ c respectively. One can show that the axial symmetry of the lattice constrains the zero field linear response such that only these two orientations give unique responses [31]. Many of the features seen in Figure 1 can be attributed to crystal field transitions of the Ho^{+3} ($^5I_8$) ions, which have been previously discussed in the context of a number of compounds [33–37]. Several of the more prominent crystal field levels are labeled in Figure 1. We discuss the details in the SI. However, abrupt changes in the spectra, including a previously undiscovered dramatic renormalization of the

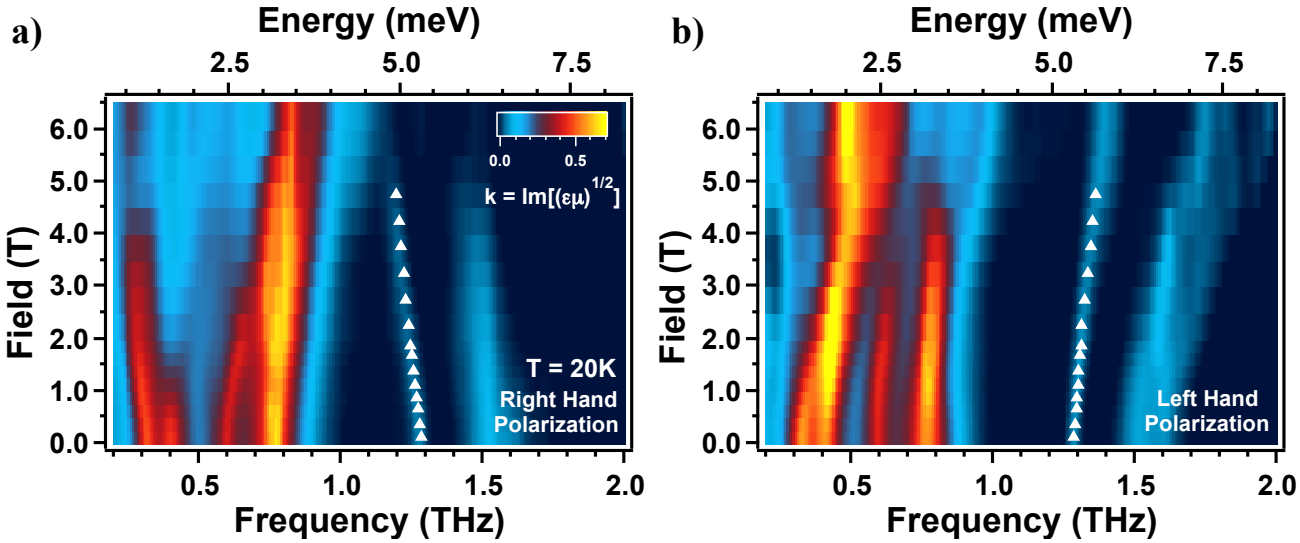

FIG. 2: Field dependence of the imaginary part of the index of refraction of HMO at 20K with the field applied along the c axis. (a) and (b) display the response to right and left hand circular polarizations respectively. The Mn AFR is the linearly varying excitation at $\approx$ 1.3 THz, which can be seen to naturally partition into low and high energy branches in the circular basis. White triangles mark the extracted resonant frequencies of the AFR.

crystal field excitation energies at $\approx$ 5K, can be used to identify the three zero field magnetic transitions at temperatures of $T_N \approx 72$K, $T_{SR} \approx 37$K, and $T_{Ho} \approx 5.25$K - in excellent agreement with previously reported values. Instead, we focus on the AFR of the Mn sublattice which is labeled "M" in Figure 1. In order to extract the dynamical properties of this mode, the spectra were fit to a general model of a Drude-Lorentz oscillator with additional linear background to account for neighboring Ho crystal field levels. White circles in Figure 1 mark the extracted resonant frequencies of the Mn AFR (See full data set in SI).

Measurements were performed as a function of magnetic field in order to investigate the field dependent splitting of the AFR. Figure 2(a,b) displays image plots of the dissipative part of the index of refraction as a function of magnetic field at 20K for right and left hand circular polarizations respectively. Again strong dissipation from Ho crystal field levels is observed below 1 THz and near 1.5 THz. The excitation whose energy is linearly dependent with magnetic field is the AFR of the Mn sublattice. One can immediately see that the two branches of the AFR possess distinct selection rules to right and left hand circular polarizations. Such a partitioning of the AFR allows unique access to the splitting of this mode in small magnetic fields, within the low field "intermediate" phase of HMO, where the two branches would otherwise be highly overlapping in the linear basis. In a similar manner as the zero field data, these spectra were fit with a model of a Lorentzian oscillator on a linear background to extract the magnetic field dependent dynamical properties of the AFR. White triangles in Figure 2(a,b) mark the extracted resonant frequencies of the AFR at fields where it is well defined.

The g-factors of the AFR can be found by fitting the extracted resonant frequencies as a function of magnetic field. To reiterate, the expectation from Equation 2 is a symmetric splitting of the two branches with g-factors $\approx \pm 1$. Figure 3(a) displays linear fits of the AFR resonant frequencies in weak magnetic fields, well within the low field phase of HMO. One can see that g-factors are large and unexpectedly *asymmetric*, with the low energy branch possessing a g-factor that is $\approx 50\%$ greater than that of the high energy branch. This asymmetry extends to negative fields as well, such that the low energy branch always possesses a larger g-factor, independent of field direction. A remarkable aspect of the data is the kink in the R and L branches as a function of B near zero field. We believe this non-analyticity results from how the ground state is selected with a change in sign of the magnetic field as discussed below. The small difference in g-factor for the low energy branches between positive and negative fields likely stems from larger error bars in negative fields due to a weak AFR in this orientation and its overlap with crystal field levels. While enhanced g-factors have been interpreted via RE-Mn spin interactions [6], asymmetry in the field dependent splitting of the AFR has not been reported previously. However, close inspection of the data of Ref. [27] reveals that the low energy branch of the AFR possesses a significantly larger g-factor than the high energy branch in $TmMnO_3$, similar to our results in HMO.

Additional information can be obtained by examining the temperature dependence of the g-factors (Fig-

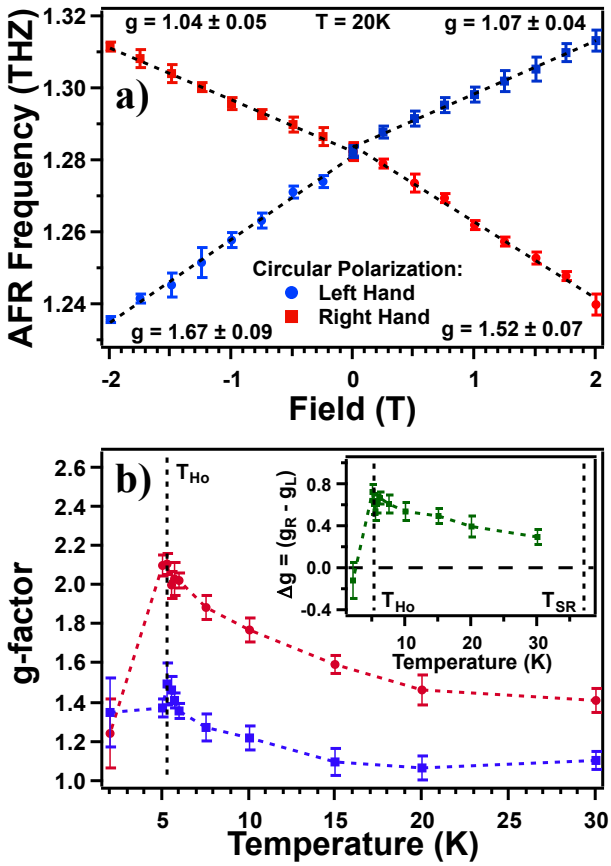

FIG. 3: (a) Resonant frequency of the AFR for both left hand (blue, circles) and right hand (red, squares) circular polarizations as a function of magnetic field at T = 20K. The low energy branch of the AFR possesses a significantly larger g-factor than that of the high energy branch, regardless of polarization or field direction. (b) Temperature dependence of the g-factors which reveals a significant renormalization at T_{Ho}, the Ho spin ordering temperature. Inset: Temperature dependence of the asymmetry in g-factors found by taking the difference of the data shown in (b). Dashed vertical lines denote the transitions at T_{Ho} and T_{SR}.

ure 3(b)). Data were only fit within the low field intermediate phase of HMO, after which the g-factors are known to change in hexagonal manganites [27]. As the temperature is decreased the g-factors increase, a trend which is consistent with other hexagonal manganites which possess rare-earth magnetism [27]. However, such experiments have yet to be performed in the vicinity of the low temperature rare-earth ordering transition of these samples. In HMO we observe a large renormalization of the g-factors at T_{Ho}, at which they increase dramatically in the vicinity of the transition and then decrease at temperatures below the transition. We observe an increase in g-factor of $\approx 35\%$ from 30K to T_{Ho} in the left hand branch, while the right hand branch shows an even larger 50% increase. This effect can be attributed to a large increase in the effective internal fields near T_{Ho}, as the Ho sublattices are more easily magnetized near the transition, consistent with the observed peak in the magnetic susceptibility at T_{Ho} [1]. Below the transition, with the Ho sublattices presumably AF ordered, the internal fields are reduced and the g-factors return close to their high temperature values (although the errors bars at 2K are large due to strong overlap with neighboring Ho crystal field levels).

The inset of Figure 3(b) displays the temperature dependence of the asymmetry in g-factors found by taking the difference of the g-factors of the high and low energy branches. Such a plot clearly demonstrates this asymmetry to be related to the Ho spins. One can see that the difference in g-factors appears to onset near T_{SR}, the temperature at which the onset of Ho spin magnetization is observed [3, 25] and presumably when the Ho spins are easily polarizable with weak magnetic fields. The asymmetry then also shows a renormalization at T_{Ho}, before dropping to nearly zero at lower temperatures.

What is the origin of the asymmetry in the AFR branches? We have explored a scenario in which paramagnetic Ho moments generate an effective exchange field on Mn sites. To tilt both AFR branches down, this exchange field $\mathbf{H}_{\text{eff}}$ must be antiparallel to Mn moments, reducing the cost of small deviations from the ordered state. At the same time, it is generated by fluctuating Ho moments whose thermal average $\langle S^z_{\text{Ho}} \rangle = \chi_{\text{Ho}} B$ is proportional to the applied field B and to the Ho magnetic susceptibility χ_{Ho}, which grows as the temperature is lowered toward the Ho ordering at T_{Ho}. An exchange field in the ab plane coming from Ho spins polarized along the c axis can come from, e.g., the Dzyaloshinskii-Moriya (DM) interaction $H_{\text{DM}} = \mathbf{D} \cdot (\mathbf{S}_{\text{Ho}} \times \mathbf{S}_{\text{Mn}})$ with a DM vector $\mathbf{D}$ in the ab plane.

Although we believe this DM term plays a role here, in the most straightforward scenario this leads to leads to the opposite effect: both AFR branches tilt up. To understand why this occurs, note that the effective exchange field $\mathbf{H}_{\text{eff}} = -\mathbf{D} \times \langle \mathbf{S}_{\text{Ho}} \rangle$ breaks the global symmetry of rotations in the ab plane manifest in the Hamiltonian (7). Mn spins orient themselves parallel to $\mathbf{H}_{\text{eff}}$ to minimize the DM energy and select a ground state. In general, it is this change in the ground state with the change in field direction that leads to the non-analyticity of the R and L excitations near B=0. Deviations from these preferred directions now cost extra energy, which leads to a hardening of both AFR branches contrary to the experimental observations. We have found that other types of interactions breaking the global rotational symmetry that select a ground state generically harden both AFR branches [38]. In order to get a softening, one must have the combined effect of both DM interaction and terms like quartic interactions that force an anisotropy in-plane. When both perturbations are present, one may select the ground state and the other determines the stiffness of the hard modes. This can cause a net softening.

See SI for further details.

In summary, high precision time domain terahertz experiments were used to probe the field dependent THz spectra of the multiferroic h-$HoMnO_3$. Through careful examination of the temperature and field dependence of an antiferromagnetic resonance of the manganese sublattice, we demonstrated exceptionally strong Ho-Mn spin interactions, including a large renormalization of the g-factors at T_{Ho}, the temperature at which Ho magnetism onsets. Although an enhancement of the g-factor through RE-Mn interactions has been inferred before [6, 27], we demonstrated that this effect changes dramatically at the RE ordering temperature. Additionally, we demonstrated an asymmetry in the g-factors of the two AFR branches which we attributed to an additional spin interaction between RE-Mn moments. Such an effect may occur in other hexagonal manganites (and may have already been observed in $TmMnO_3$), as those which possess rare earth magnetism display similar spin reorientation transitions. Our analysis suggests the need for additional experiments and theoretical investigations into the RE-Mn spin interactions of these hexagonal manganites.

Research at JHU was funded by the U.S. Department of Energy, Office of Basic Energy Sciences, Division of Materials Sciences and Engineering through Grant No. DE-FG02-08ER46544. Work at Rutgers was supported by the DOE under Grant No. DOE: DE-FG02-07ER46382. NJL acknowledges additional support through the ARCS Foundation Dillon Fellowship. We would like to thank C. Broholm for helpful conversations.

[1] B. Lorenz, ISRN Condensed Matter Physics **vol. 2013** (2013).
[2] N. Hur, I. K. Jeong, M. F. Hundley, S. B. Kim, and S.-W. Cheong, Phys. Rev. B **79**, 134120 (2009).
[3] S. Nandi, A. Kreyssig, L. Tan, J. W. Kim, J. Q. Yan, J. C. Lang, D. Haskel, R. J. McQueeney, and A. I. Goldman, Phys. Rev. Lett. **100**, 217201 (2008).
[4] M. Fiebig, C. Degenhardt, and R. V. Pisarev, Phys. Rev. Lett. **88**, 027203 (2001).
[5] X. Fabrèges, I. Mirebeau, P. Bonville, S. Petit, G. Lebras-Jasmin, A. Forget, G. André, and S. Pailhès, Phys. Rev. B **78**, 214422 (2008).
[6] D. Talbayev, A. D. LaForge, S. A. Trugman, N. Hur, A. J. Taylor, R. D. Averitt, and D. N. Basov, Phys. Rev. Lett. **101**, 247601 (2008).
[7] D. Meier, H. Ryll, K. Kiefer, B. Klemke, J.-U. Hoffmann, R. Ramesh, and M. Fiebig, Phys. Rev. B **86**, 184415 (2012).
[8] S. G. Condran and M. L. Plumer, Journal of Physics: Condensed Matter **22**, 162201 (2010).
[9] T. Lottermoser, T. Lonkai, U. Amann, D. Holhwein, J. Ihringer, and M. Fiebig, Nature **430**, 541 (2003).
[10] B. G. Ueland, J. W. Lynn, M. Laver, Y. J. Choi, and S.-W. Cheong, Phys. Rev. Lett. **104**, 147204 (2010).
[11] B. Lorenz, A. P. Litvinchuk, M. M. Gospodinov, and C. W. Chu, Phys. Rev. Lett. **92**, 087204 (2004).
[12] C. dela Cruz, F. Yen, B. Lorenz, Y. Q. Wang, Y. Y. Sun, M. M. Gospodinov, and C. W. Chu, Phys. Rev. B **71**, 060407 (2005).
[13] N. Iwata and K. Kohn, Journal of the Physical Society of Japan **67**, 3318 (1998).
[14] F. Yen, C. R. dela Cruz, B. Lorenz, Y. Y. Sun, Y. Q. Wang, M. M. Gospodinov, and C. W. Chu, Phys. Rev. B **71**, 180407 (2005).
[15] S.-W. Cheong and M. Mostovoy, Nat. Mater. **6**, 13 (2007).
[16] B. B. Van Aken, T. T. M. Palstra, A. Filippetti, and A. Nicola, Nat. Mater. **3**, 164 (2004).
[17] C. J. Fennie and K. M. Rabe, Phys. Rev. B **72**, 100103 (2005).
[18] M. Fiebig, D. Fröhlich, K. Kohn, S. Leute, T. Lottermoser, V. V. Pavlov, and R. V. Pisarev, Phys. Rev. Lett. **84**, 5620 (2000).
[19] M. Fiebig, C. Degenhardt, and R. V. Pisarev, Journal of Applied Physics **91**, 8867 (2002).
[20] M. Fiebig, T. Lottermoser, and R. V. Pisarev, Journal of Applied Physics **93**, 8194 (2003).
[21] O. P. Vajk, M. Kenzelmann, J. W. Lynn, S. B. Kim, and S.-W. Cheong, Phys. Rev. Lett. **94**, 087601 (2005).
[22] P. J. Brown and T. Chatterji, Journal of Physics: Condensed Matter **18**, 10085 (2006).
[23] P. J. Brown and T. Chatterji, Phys. Rev. B **77**, 104407 (2008).
[24] H. Sugie, N. Iwata, and K. Kohn, Journal of the Physical Society of Japan **71**, 1558 (2002).
[25] T. Lonkai, D. Hohlwein, J. Ihringer, and W. Prandl, Applied Physics A **74** (2002).
[26] W. Palme, F. Mertens, O. Born, and B. L uthi, Solid State Commun. **76**, 873 (1990).
[27] E. C. Standard, T. Stanislavchuk, A. A. Sirenko, N. Lee, and S.-W. Cheong, Phys. Rev. B **85**, 144422 (2012).
[28] I. Dzyaloshinsky, Journal of Physics and Chemistry of Solids **4**, 241 (1958).
[29] T. Moriya, Phys. Rev. **120**, 91 (1960).
[30] N. J. Laurita, B. Cheng, R. Barkhouser, V. A. Neumann, and N. P. Armitage, Journal of Infrared, Millimeter, and Terahertz Waves pp. 1–9 (2016).
[31] N. P. Armitage, Phys. Rev. B **90**, 035135 (2014).
[32] C. M. Morris, R. V. Aguilar, A. V. Stier, and N. P. Armitage, Opt. Express **20**, 12303 (2012).
[33] B. R. Judd, Proceedings of the Royal Society of London A: Mathematical, Physical and Engineering Sciences **232**, 458 (1955).
[34] A. Abragam and B. Bleaney, *Electron Paramagnetic Resonance* (Clarendon Press, Oxford, 1970).
[35] R. J. Elliott and K. W. H. Stevens, Proceedings of the Royal Society of London A: Mathematical, Physical and Engineering Sciences **218**, 553 (1953).
[36] S. Rosenkranz, A. P. Ramirez, A. Hayashi, R. J. Cava, R. Siddharthan, and B. S. Shastry, Journal of Applied Physics **87**, 5914 (2000).
[37] U. Ranon and K. Lee, Phys. Rev. **188**, 539 (1969).
[38] See Supplemental Information.
[39] K. Momma and F. Izumi, Journal of Applied Crystallography **44**, 1272 (2011).
[40] P. Coeure and *et al.*, Proc. of 1st Intl. Meeting on Ferroelectricity (Institute of Physics, Czech. Acad. Sci., Prague), p. 332 (1966).
[41] R. C. Jones, J. Opt. Soc. Am. **31**, 488 (1941).

[42] A. Altland and B. D. Simons, *Condensed Matter Field Theory* (Cambridge University Press, New York, 2010), 2nd ed., ISBN 978-0521769754.
[43] S. G. Condran and M. L. Plumer, J. Phys.: Condens. Matter **22**, 162201 (2010).
[44] K. Stevens, Physics Letters A **47**, 401 (1974), ISSN 0375-9601.
[45] A. A. Sirenko, S. M. O'Malley, K. H. Ahn, S. Park, G. L. Carr, and S.-W. Cheong, Phys. Rev. B **78**, 174405 (2008).

SUPPLEMENTARY INFORMATION FOR "ANOMALOUS EXCHANGE INTERACTIONS BETWEEN RE^{+3} AND MN^{+3} MOMENTS IN MULTIFERROIC H-$REMNO_3$"

CRYSTAL STRUCTURE OF HMO

Above the ferroelectric transition temperature, $T_c = 875$K, the inversion symmetric hexagonal lattice of h-$HoMnO_3$ (HMO) is composed of alternating layers within the a-b plane of corner sharing MnO_5 bipryamids and Ho^{+3} ions. These layers are stacked and well separated along the c axis. At the ferroelectric transition, the MnO_5 bipryamids buckle due to structural trimerization [15–17] resulting in opposite displacements of 1/3 and 2/3 of the Ho^{+3} ions respectively. Figure 4 displays the crystal structure of HMO in the ferroelectric phase with views along the (left) c axis and (right) a axis of the crystal respectively [39]. The corresponding symmetry of the lattice is reduced to the non-centrosymmetric polar space group $P6_3cm$ with a net polarization formed along the hexagonal c direction [40].

The complexity of the magnetism of HMO can also be inferred from its crystal structure. The two Ho positions, the 2a (green) and 4b (blue) sites of the lattice, are symmetry distinct with point group symmetries of C_{3v} and C_3 respectively. Therefore HMO possesses a total of five unique magnetic sublattices, the three Mn sublattices which form a frustrated triangular layer and the two symmetry distinct Ho sublattices. With such low symmetry, the structure can in principle support a wide array of magnetic exchange mechanisms within and between these sublattices as evidenced by the complexity of the magnetic phase diagram of HMO [21].

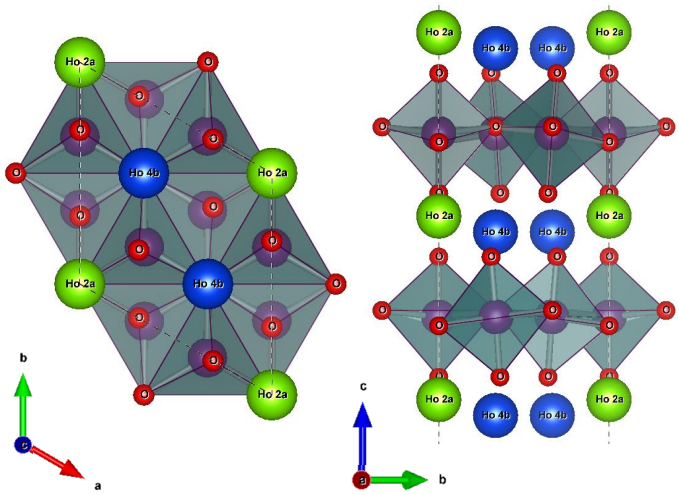

FIG. 4: Crystal structure of HMO in the ferroelectric phase, $T < T_c$=875K, with views along the (left) c axis and (right) a axis of the crystal. In this phase, the two Ho^{+3} sites of the lattice, which are shown in green and blue respectively, posses different point group symmetries.

THE TRANSMISSION MATRIX IN THE LINEAR AND CIRCULAR BASES

In this section we detail the analysis of our time-domain terahertz (TDTS) data in both the linear and circular bases. TDTS is a high resolution method for accurately measuring the electromagnetic response of a sample in the experimentally challenging THz range. In a typical TDTS experiment, the electric field of a transmitted THz pulse through a sample is measured as a function of real time. Fourier transforming the measured electric field and referencing to an aperture of identical size allows access to the frequency dependent *complex* transmission spectrum

of the sample which, in the limit of $\tilde{\epsilon} \gg \tilde{\mu}$, is given by:

$$\widetilde{T} = \frac{4\widetilde{n}}{(\widetilde{n}+1)^2} \exp\left[\frac{i\omega d}{c}(\widetilde{n}-1)\right] \tag{3}$$

where d is the sample thickness, ω is the frequency, c is the speed of light, $\widetilde{n}$ is the sample's complex index of refraction, and normal incidence has been assumed. One can then numerically invert the transmission to obtain both the frequency dependent real and imaginary parts of the index of refraction. In principle the index of refraction, $\widetilde{n} = n + ik = \sqrt{\widetilde{\epsilon}\widetilde{\mu}}$, contains both the electric and magnetic responses of the sample as THz fields can couple to both electric and magnetic dipole transitions. Thus, electric and magnetic effects can be difficult to separate in such a single pass transmission experiment. This is further complicated by the strong multiferroic and magnetoelectric coupling of HMO which introduces an additional term into the index of refraction. Therefore, we neglect to attempt to identify features in the spectra as purely electric or magnetic in origin and instead report the combined response in the form of the imaginary, or dissipative, part of the index of refraction.

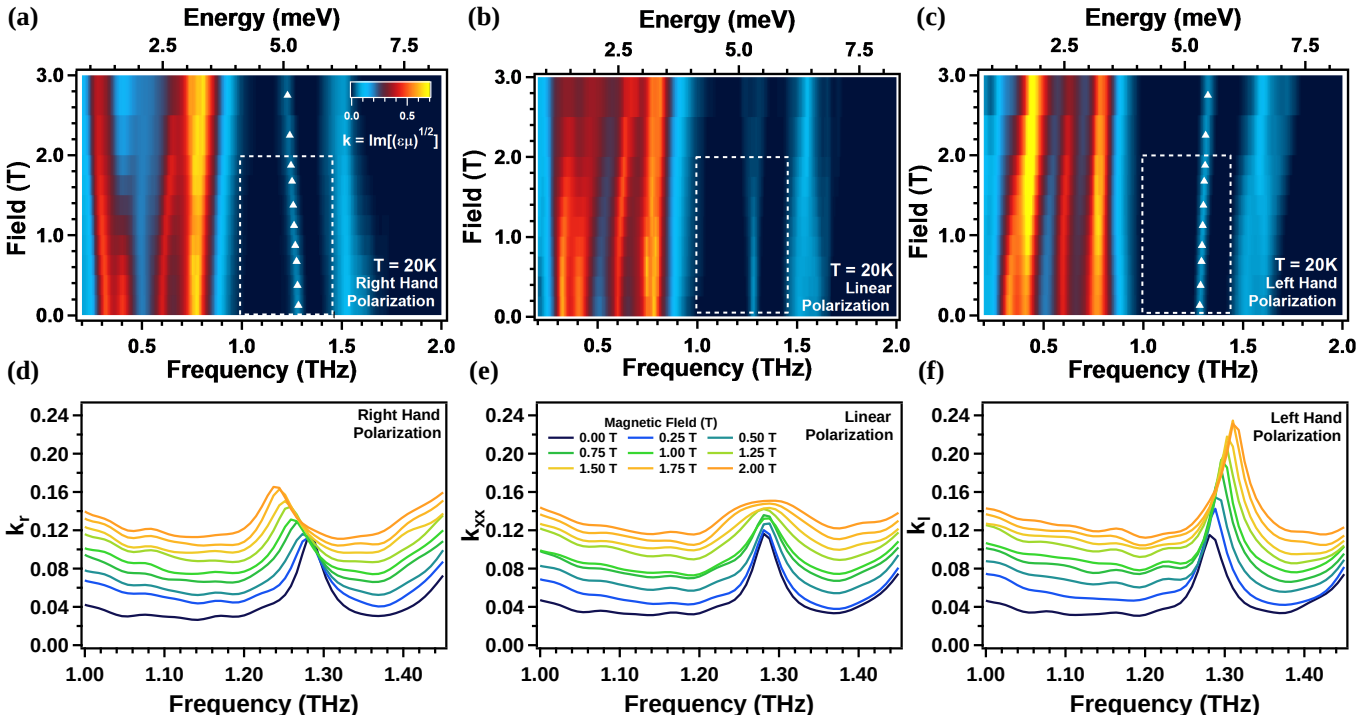

FIG. 5: Image plots of the dissipative part of the index of refraction in both the (b) linear basis and the (a) right and (c) left hand channels of the circular basis within the low field "intermediate" phase of HMO. (d)-(f) Plots of the dissipative part of the index of refraction within the dotted white box of the image plots shown in (a)-(c). The advantage of converting to the circular basis is immediately apparent, as both modes of the AFR highly overlap in the linear basis but are naturally partitioned into the right and left hand channels of the circular basis.

In the Jones calculus [41], the full linear response of the sample is represented as a complex 2×2 transmission matrix which transforms the incident electric field ($\tilde{\mathbf{E}}_{\text{in}}$) of THz light, written in the linear basis, as:

$$\begin{bmatrix} \tilde{E}_{\text{x,out}} \\ \tilde{E}_{\text{y,out}} \end{bmatrix} = \begin{bmatrix} \tilde{T}_{xx} & \tilde{T}_{yx} \\ \tilde{T}_{xy} & \tilde{T}_{yy} \end{bmatrix} \begin{bmatrix} \tilde{E}_{\text{x,in}} \\ \tilde{E}_{\text{y,in}} \end{bmatrix} \tag{4}$$

In the most general case the transmission matrix contains four independent components as shown above and one must vary the incident and detected polarization of light to measure individual elements of the transmission matrix. However, Neumann's principle ensures that the transmission matrix must also possess the symmetries inherent to the crystal itself [31], which often results in degeneracies between elements of the transmission matrix. Such degeneracies can be exploited to measure samples in the basis in which the transmission matrix is diagonalized, and therefore the natural eigenpolarizations of the crystal.

TDTS experiments performed as a function of magnetic field were done so in the Faraday geometry, in which $\vec{\text{k}}_{\text{THz}} \parallel \vec{\text{H}}_{\text{dc}} \parallel \hat{z}$, on a HMO sample oriented such that $c \parallel \hat{z}$. In this case, the crystal structure is symmetric under rotations

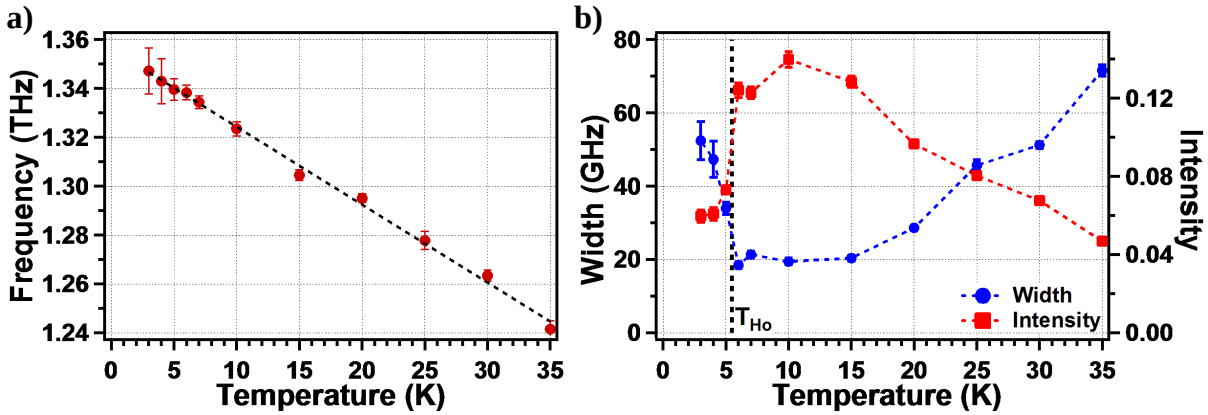

FIG. 6: Temperature dependent dynamical properties of the Mn AFR for temperatures below T_{SR}. (left) Resonant frequency. (right) Width (blue squares, left axis) and intensity (red circles, right axis).

of 120° about the $\hat{z}$ axis. The transmission matrix must therefore also obey this symmetry, which greatly constrains its form such that it must be fully antisymmetric with only two unique components:

$$\tilde{T}_{\text{linear}} = \begin{bmatrix} \tilde{T}_{xx} & \tilde{T}_{xy} \\ -\tilde{T}_{xy} & \tilde{T}_{xx} \end{bmatrix} \tag{5}$$

Such a fully antisymmetric transmission matrix can be diagonalized by a circular basis transformation as:

$$\tilde{T}_{\text{circular}} = \begin{bmatrix} \tilde{T}_{xx} + i \cdot \tilde{T}_{xy} & 0 \\ 0 & \tilde{T}_{xx} - i \cdot \tilde{T}_{xy} \end{bmatrix} = \begin{bmatrix} \tilde{T}_r & 0 \\ 0 & \tilde{T}_l \end{bmatrix} \tag{6}$$

where $\tilde{T}_l$ and $\tilde{T}_r$ refer to the transmission of left and right hand circularly polarized light, the eigenpolarizations for this orientation, respectively. The above analysis suggests that experiments performed in Faraday geometry are best understood in the circular basis.

As we demonstrated in the main text such a conversion to the circular basis can be highly advantageous in the study of magnetic excitations. Figure 5 displays magnetic field dependent data in both the linear and circular basis to demonstrate the advantage of such a transformation. Shown are image plots of the imaginary part of the index of refraction in the (b) linear and (a) right hand and (c) left hand circular polarizations. Plots (d)-(f) display the data in the regions marked by the white dotted boxes of (a)-(c), the range fit to extract the g-factors in Figure 3(a) of the main text. One can see the difficulty in extracting the resonant frequencies of both branches of the AFR in the linear basis, as the field dependent splitting is far smaller than the excitation width such that the two branches of the AFR highly overlap, even at fields as large as a few Tesla. With such a complex magnetic field dependent phase diagram as HMO [21], the study of the AFR in the low field phase has been previously impossible. However, the high and low energy branches of the AFR naturally partition into left and right hand circular polarizations respectively in the circular basis, allowing for determination of their resonant frequencies and g-factors with exceptional precision in weak magnetic fields. We expect such a transformation to be similarly beneficial to the study of other hexagonal manganites as well, thus providing a paradigm for the optical study of the AFR in these and other classes of materials.

TEMPERATURE AND FIELD DEPENDENCE OF THE MN AFR

The temperature dependence of the resonant frequency of the Mn AFR has been previously investigated in several hexagonal manganites [27]. In these systems it was empirically found that the AFR frequency displays a power law dependence with temperature as $\omega(T) = \omega(0) + aT^b$, where the exponent b was found to be ≈ 3. Deviations from this power law behavior at low temperatures were observed in hexagonal manganites with rare-earth magnetism and were interpreted as corresponding to the onset of rare-earth moment fluctuations and therefore RE-Mn interactions.

Figure 6(a) displays the resonant frequency of the AFR in HMO for temperatures below T_{SR}, extracted by fitting the spectra as described in the main text. One can see that in contrast to other hexagonal manganites, the AFR frequency in HMO displays a linear dependence ($b = 1.02$) with temperature. This is consistent with the onset of

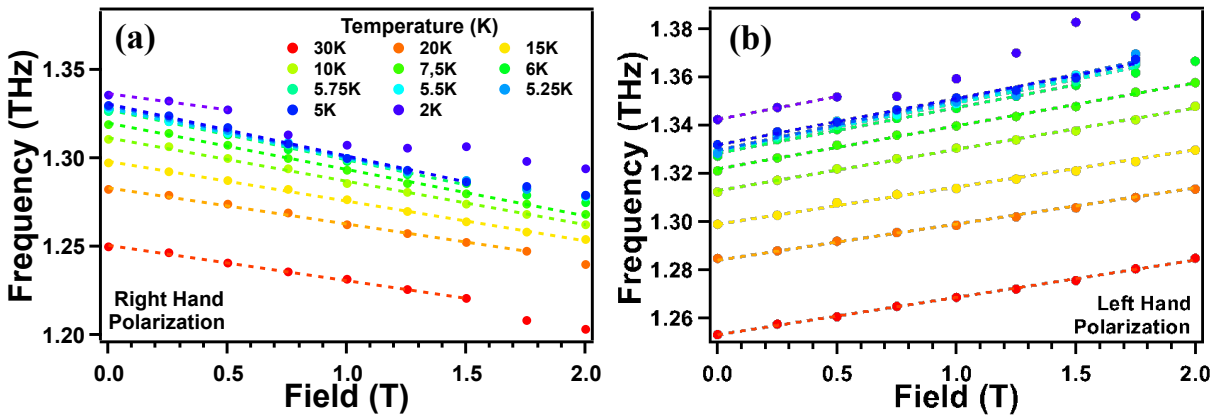

FIG. 7: Field dependence of the Mn AFR resonant frequency in the right and left hand channels of the circular basis. Data is shown below 2T, where the highest signal to noise is achieved and well within the low field phase of HMO. Dotted lines are the resultant linear fit of the data at each temperature.

magnetic fluctuations of at least one of the Ho sublattices at T_{SR}, in agreement with previous reports [3, 25] and our own analysis presented in the main text. Figure 6(b) displays the temperature dependence of the width (blue, left axis) and intensity (red, right axis) of the AFR for temperatures below T_{SR}. One can see that as the temperature is reduced the AFR becomes more well defined, displaying both an increase in intensity and narrowing. However, at T_{Ho} the AFR is dramatically damped and the intensity is significantly reduced. The origin of such an effect is currently unclear but one possible explanation is that the Mn AFR hybridizes with nearly degenerate Ho crystal field levels below T_{Ho}. If so, then HMO may display the first hybridized magnon-crystal field excitations which originate from distinct magnetic sublattices. Further research is required to confirm such a possibility.

Figure 7 displays the AFR resonant frequency as a function of magnetic field for temperatures below T_{SR} for both the (a) right hand and (b) left hand circular polarizations. Markers denote the extracting resonant frequency found by fitting the data described in the text while dotted lines represent linear fits of the data from which the g-factors were extracted. It was previously found that the g-factors of the Mn AFR change significantly in the "high field" phase of hexagonal manganites, i.e. for field $H > H_c \approx 3$ T [27]. Therefore, care was taken to only include data taken within the low field "intermediate" phase to obtain the g-factors. Such phase boundaries were identified by obvious non-linearities in our data as well as published phase boundaries found previously in HMO [21].

SPIN WAVES IN AN EASY-PLANE TRIANGULAR ANTIFERROMAGNET

Spin Lagrangian

We first derive the frequency of the antiferromagnetic resonance in an easy-plane triangular antiferromagnet in the presence of a weak magnetic field normal to the easy plane. The spin Hamiltonian is

$$H = J\sum_{\langle ij\rangle}\mathbf{S}_i\cdot\mathbf{S}_j + \Delta\sum_i (S_i^z)^2 + g\mu_B\mathbf{B}\cdot\sum_i\mathbf{S}_i, \tag{7}$$

Here $J > 0$ is the nearest-neighbor exchange coupling, $\Delta > 0$ is the strength of easy-plane anisotropy, g is the Landé gyromagnetic factor, μ_B is the Bohr magneton, and $\mathbf{B} = (0, 0, B)$ is an external magnetic field. The index i is summed over all spins, $\langle ij\rangle$ over all nearest-neighbor pairs of spins. We treat the spins as classical vectors of fixed length $\hbar S$ and parametrize them in terms of spherical angles θ_i and ϕ_i in the global frame xyz:

$$\mathbf{S}_i = S(\sin\theta_i\cos\phi_i, \sin\theta_i\sin\phi_i, \cos\theta_i). \tag{8}$$

In equilibrium, the spins form an ordered pattern with three sublattices $n = 1, 2, 3$ (Fig. 8):

$$\cos\theta_n = \frac{g\mu_B B}{(9J + 2\Delta)S}, \quad \phi_n = \phi_z + \frac{2\pi n}{3}, \tag{9}$$

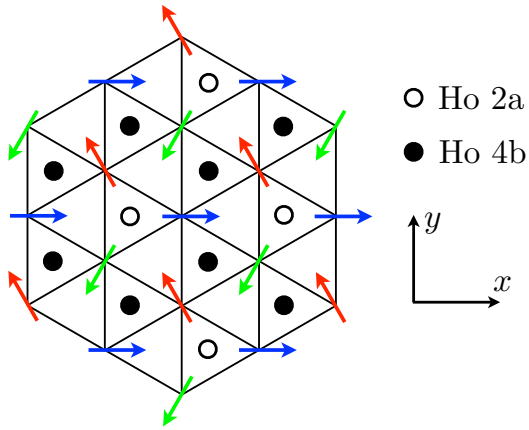

FIG. 8: The 3-sublattice antiferromagnetic order on the Mn lattice (red, green, and blue arrows) and the two types of Ho ions, 2a (open circles) and 4b (filled circles).

A spin on one sublattice has three neighbors from each of the other sublattices. The offset angle ϕ_z represents the global symmetry of rotations about the hard axis z.

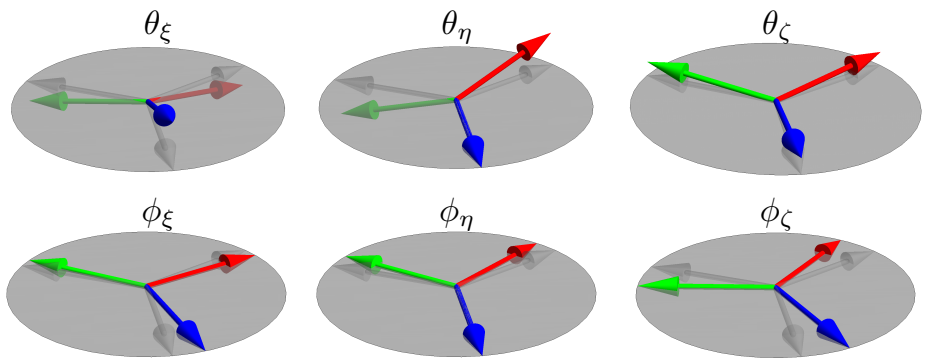

FIG. 9: Normal modes of a triangular antiferromagnet. In zero field, the three sublattice spins $\mathbf{S}_1$ (red), $\mathbf{S}_2$ (green), and $\mathbf{S}_3$ (blue) lie in the easy plane xy (gray). Faint arrows represent an equilibrium state with the spins in the easy plane and pointing at 120° to one another. The θ and ϕ modes move the spins in the polar and azimuthal directions, respectively. The spin axes ξ and η point along $\mathbf{S}_2 - \mathbf{S}_1$ and $\mathbf{S}_3$, respectively. The ζ axis coincides with the hard axis z.

The dynamics of small-amplitude spin waves with $\mathbf{q} = 0$ is most readily obtained from the Lagrangian

$$L = \hbar S \sum_{n=1}^{3} (\cos\theta_n - 1)\dot{\phi}_n - U(\{\theta, \phi\}). \tag{10}$$

The first term in the Lagrangian represents the geometric (Berry-phase) part of the spin action [42], the second is potential energy.

Spin waves

For small deviations from equilibrium, we introduce normal coordinates representing eigenmodes:

$$\begin{pmatrix} \delta\theta_1 \\ \delta\theta_2 \\ \delta\theta_3 \end{pmatrix} = \begin{pmatrix} \frac{1}{2} & -\frac{\sqrt{3}}{2} & -\frac{1}{3} \\ \frac{1}{2} & \frac{\sqrt{3}}{2} & -\frac{1}{3} \\ -1 & 0 & -\frac{1}{3} \end{pmatrix} \begin{pmatrix} \theta_\xi \\ \theta_\eta \\ \theta_\zeta \end{pmatrix}, \qquad \begin{pmatrix} \delta\phi_1 \\ \delta\phi_2 \\ \delta\phi_3 \end{pmatrix} = \begin{pmatrix} -\frac{1}{3} & \frac{1}{\sqrt{3}} & 1 \\ -\frac{1}{3} & -\frac{1}{\sqrt{3}} & 1 \\ \frac{2}{3} & 0 & 1 \end{pmatrix} \begin{pmatrix} \phi_\xi \\ \phi_\eta \\ \phi_\zeta \end{pmatrix} \tag{11}$$

For convenience, we have introduced a new frame $\xi\eta\zeta$ defined by the ordered state (Fig. 9). The normal modes have the following meanings in the absence of the applied field. θ_ζ describes the average latitude of the three sublattice

spins; thus $\hbar S\theta_\zeta$ is the net spin in the ζ direction, a momentum conjugate to the global rotation angle ϕ_ζ in the easy plane. (The mode ϕ_ζ is redundant as it globally rotates all spins about the hard axis, thus playing the same role as ϕ_z does.) Global rotations tilting the spins out of the easy plane are quantified by angles θ_ξ and θ_η about the respective spin axes. Lastly, ϕ_ξ and ϕ_η represent deformations of the 120° order within the easy plane and create a net spin with projections $-\hbar S\phi_\xi$ and $-\hbar S\phi_\eta$, onto the ξ and η axes respectively.

To the second order in the normal coordinates and to the first order in the magnetic field B,

$$L = \hbar S(\theta_\xi\dot{\phi}_\xi + \theta_\eta\dot{\phi}_\eta + \theta_\zeta\dot{\phi}_\zeta) - U, \tag{12}$$

where

$$U = \frac{3JS^2}{2}\left(\phi_\xi^2 + \phi_\eta^2\right) + \frac{3\Delta S^2}{2}\left(\theta_\xi^2 + \theta_\eta^2\right) + \tilde{g}\mu_B BS\left(\theta_\xi\phi_\eta - \theta_\eta\phi_\xi\right) + \frac{(9J + 2\Delta)S^2}{6}\theta_\zeta^2 \tag{13}$$

is the potential energy and

$$\tilde{g} = \frac{g}{2(1 + 2\Delta/9J)} \tag{14}$$

is an effective Landé gyromagnetic factor.

As expected, the soft mode ϕ_ζ does not influence the potential energy and its conjugate momentum $\hbar S\theta_\zeta$ is a conserved quantity. These two coordinates represent the Goldstone mode with frequency $\omega = 0$ in the limit $\mathbf{q} \to 0$.

The equations of motion for the remaining four coordinates are

$$\hbar\frac{d}{dt}\begin{pmatrix}\theta_\xi\\ \phi_\xi\\ \theta_\eta\\ \phi_\eta\end{pmatrix} = \begin{pmatrix}0 & -3JS & \tilde{g}\mu_B B & 0\\ 3\Delta S & 0 & 0 & \tilde{g}\mu_B B\\ -\tilde{g}\mu_B B & 0 & 0 & -3JS\\ 0 & -\tilde{g}\mu_B B & 3\Delta S & 0\end{pmatrix}\begin{pmatrix}\theta_\xi\\ \phi_\xi\\ \theta_\eta\\ \phi_\eta\end{pmatrix} \tag{15}$$

In zero magnetic field, there are two degenerate magnons with energy $\hbar\omega(0) = 3S\sqrt{J\Delta}$, one involving θ_ξ and ϕ_ξ, the other θ_η and ϕ_η. The field couples the two modes, lifting the degeneracy. The eigenmodes and eigenfrequencies are

$$\begin{pmatrix}\theta_\xi\\ \phi_\xi\\ \theta_\eta\\ \phi_\eta\end{pmatrix} = \begin{pmatrix}\sqrt{J}\cos\omega t\\ \sqrt{\Delta}\sin\omega t\\ \sqrt{J}\cos(\omega t \pm \pi/2)\\ \sqrt{\Delta}\sin(\omega t \pm \pi/2)\end{pmatrix}, \qquad \hbar\omega_\pm(B) = 3S\sqrt{J\Delta} \pm \tilde{g}\mu_B B. \tag{16}$$

The in-plane components of spin, $\hbar\mathbf{S}_\perp = -\hbar S(\phi_\xi, \phi_\eta, 0)$ in the $\xi\eta\zeta$ frame, rotate clockwise or counterclockwise, generating circularly polarized electromagnetic waves. The straight lines $\omega_\pm(B)$ have equal and opposite slopes $d\omega_\pm/dB = \pm\tilde{g}\mu_B/\hbar$.

Different slope magnitudes will result if we modify the first two terms in the potential energy (13) so that their coefficients depend linearly on B. We may replace

$$J \mapsto J(B) \equiv J + J'B, \quad \Delta \mapsto \Delta(B) \equiv \Delta + \Delta' B. \tag{17}$$

Then, to the linear order in B, the eigenfrequencies will be

$$\omega_\pm(B) = \omega(0) + \omega(0)\left(\frac{J'}{2J} + \frac{\Delta'}{2\Delta}\right)B \pm \tilde{g}\mu_B B \tag{18}$$

and the slopes $d\omega_\pm/dB$ will differ in magnitude.

Dzyaloshinskii-Moriya interaction between Ho and Mn spins

One of the mechanisms that could create a difference in the slopes $d\omega_\pm/dB$ is the Dzyaloshinskii-Moriya (DM) interaction $\mathbf{D}\cdot(\mathbf{S}_{\rm Ho}\times\mathbf{S}_{\rm Mn})$ between Ho and Mn spins. At intermediate temperatures, Ho spins remain disordered but are magnetized by the applied magnetic field, $\mathbf{s} = \chi\mathbf{B}$, where χ is the Ho susceptibility. With the Ho spins magnetized along the applied field (along the hard axis z), we only need to consider the transverse x and y components of the

DM vector $\mathbf{D}$. They generate an effective magnetic field on an Mn site $\mathbf{h}_{\rm DM} = -\mathbf{D} \times \langle \mathbf{S}_{\rm Ho} \rangle$ oriented in the easy plane xy. For a given Mn site, the fields from the adjacent Ho ions vary in orientation.

If all six adjacent Ho ions (three above and three below an Mn plane) were equivalent and located symmetrically, the Mn site would possess a threefold rotational symmetry and the net $\mathbf{h}_{\rm DM}$ would vanish. However, a lattice distortion breaks the symmetry and creates inequivalent Ho sites known as 2a and 4b. Each Mn has two 2a and four 4b Ho neighbors. As a result, the effective field $\mathbf{h}_{\rm DM}$ can be nonzero. Its orientation is restricted to the vertical plane containing the Mn ion and both of its 2a Ho neighbors, while its magnitude $h_{\rm DM} = C_{\rm DM} B$, where $C_{\rm DM}$ is a constant.

The in-plane effective field $\mathbf{h}_{\rm DM}$ breaks the global rotational invariance with respect to z-axis rotations and selects a unique ground state, in which each Mn spin points along its local effective field $\mathbf{h}_{\rm DM}$. It adds the following term to the spin energy, to second order in the normal modes of interest:

$$U_{\rm DM} = C_{\rm DM} B \cos\phi_z \left[-3 + \frac{3}{4}(\theta_\xi^2 + \theta_\eta^2) + \frac{1}{3}(\phi_\xi^2 + \phi_\eta^2) \right]. \tag{19}$$

Depending on the sign of the effective field $h_{\rm DM} = C_{\rm DM} B$, it selects the ground state with the global rotation angle $\phi_z = 0$ (if $C_{\rm DM} B > 0$) or $\phi_z = \pi$ (if $C_{\rm DM} B < 0$). The four modes stiffen:

$$U_{\rm DM} = |C_{\rm DM} B| \left[-3 + \frac{3}{4}(\theta_\xi^2 + \theta_\eta^2) + \frac{1}{3}(\phi_\xi^2 + \phi_\eta^2) \right]. \tag{20}$$

Thus the presence of the DM interaction alone does not explain the softening of the two resonance branches $\omega_\pm(B)$.

Quartic spin interactions

Another route to an asymmetric splitting of the resonance is offered by higher-order spin interactions proposed by Condran and Plumer [43] that couples the out-of-plane component of Ho spins to the in-plane components of Mn spins:

$$U_4 = K \sum_{\langle \rm HoMn \rangle} S_{\rm Ho}^z \prod_{n=1}^{3} (\mathbf{S}_{\rm Mn} \cdot \mathbf{e}_n), \tag{21}$$

with the unit vectors

$$\mathbf{e}_n = \left(\cos\frac{2\pi n}{3}, \sin\frac{2\pi n}{3}, 0 \right) \tag{22}$$

in the global frame xyz. This quartic spin interaction, introduced on phenomenological grounds, is compatible the time reversal and D_{3h} point-group symmetries. (Here we neglect the distortion creating inequivalent 2a and 4b Ho sites.)

In an applied magnetic field $\mathbf{B} = (0, 0, B)$, the energy of the modes of interest has the following additions:

$$U_4 = C_4 B \cos 3\phi_z \left[-\frac{3}{4} + \frac{9}{16}(\theta_\xi^2 + \theta_\eta^2) + \frac{3}{4}(\phi_\xi^2 + \phi_\eta^2) \right]. \tag{23}$$

The Mn spins now have three possible ground states. Depending on the sign of the prefactor $C_4 B$, the energy is minimized by the global azimuthal angles $\phi_z = 0, \pm\frac{2\pi}{3}$ (if $C_4 B > 0$) or $\phi_z = \pi, \pm\frac{\pi}{3}$ (if $C_4 B < 0$). In both cases, the AFR modes stiffen:

$$U_4 = |C_4 B| \left[-\frac{3}{4} + \frac{9}{16}(\theta_\xi^2 + \theta_\eta^2) + \frac{3}{4}(\phi_\xi^2 + \phi_\eta^2) \right]. \tag{24}$$

Combined interactions

Although neither interaction alone is capable of reproducing the experimentally observed softening of both AFR branches, their combination can, at least in principle. When both perturbations are present, one of them may select the ground state and the other determines the stiffness of the hard modes. This is possible because the DM energy (19) has a relatively large zeroth-order term, whereas the quartic interaction (23) has larger quadratic terms.

For example, let us take $C_{\rm DM} > 0$ and $C_4 = -2C_{\rm DM} < 0$. The DM term dominates in selecting the ground state with $\phi_z = 0$ (for $B > 0$). The energy of the AFR modes is

$$U_{\rm DM} + U_4 = |C_{\rm DM} B| \left[-\frac{3}{2} - \frac{3}{8}(\theta_\xi^2 + \theta_\eta^2) - \frac{7}{6}(\phi_\xi^2 + \phi_\eta^2) \right]. \tag{25}$$

The quadratic terms are expressly negative, so both AFR branches soften.

Other interactions may be combined for a similar effect. For example, a quartic DM term $\mathbf{D}' \cdot (\mathbf{S}_{\rm Ho} \times \mathbf{S}_{\rm Mn}) S_{\rm Mn}^2$ would create a potential

$$U = -\frac{3}{2} C'_{\rm DM} B \cos\phi_z (\theta_\xi^2 + \theta_\eta^2). \tag{26}$$

DESCRIPTION OF THE CRYSTAL FIELD SPECTRUM

Crystal Field Theory

As discussed in the main text, many of the excitations observed in our optical experiments can be attributed to crystal field excitations of the Ho^{+3} ($^5I_8$) ions. To date the crystal field spectrum of HMO is not well understood. In this section we describe some of the basic theoretical expectations of the Ho^{+3} ($^5I_8$) crystal field spectrum before detailing our experimental observations in the next section. We hope that our experimental results will inspire further interest in the field and temperature dependence of the crystal field levels in HMO.

We can begin to understand the crystal field spectrum of the Ho^{+3} ions by examining the relevant energy scales sequentially. One expects spin orbit coupling to be the dominant energy scale in $4f$ electron systems due to the large mass and correspondingly high atomic number of rare earth ions. Assuming pure LS-coupling, the ground state of the Ho^{+3} ions are determined by Hund's rules to be $^5I_8$. With only spin orbit coupling considered, all the states within the J=8 manifold are degenerate and well separated from the nearest J=7 manifold of states. The next largest expected energy scale is that imposed by the surrounding crystal field. However, the energy scale of the crystal field is expected to be two orders of magnitude weaker than that of spin-orbit coupling. Thus, one can treat the crystal field potential as a perturbation on the J=8 manifold. In the point charge limit, the resulting calculation shows that the crystal field breaks the degeneracy of the J=8 manifold by coupling eigenstates of the $\hat{J}_z$ operator, depending directly on the symmetry of the crystal field at the rare earth site.

As described above, the 2a and 4b Ho^{+3} sites of the lattice are symmetry distinct, possessing C_{3v} and C_3 point group symmetries respectively. The effects of such crystal fields on the $^5I_8$ ground state of Ho^{+3} have previously been studied in the double nitrates [33], the ethysulphates [34, 35], the pyrochlore magnet $Ho_2Ti_2O_7$ [36], and in Ho^{+3} doped SrF_2 [37]. In these cases the crystal field potentials, $V_{\rm CF}$, for both symmetries are easily understood in Stevens notation [44] as:

$$V_{c_3} = B_0^2 O_0^2 + B_0^4 O_0^4 + B_0^6 O_0^6 + B_6^6 O_6^6 \tag{27}$$

$$V_{c_{3v}} = B_0^2 O_0^2 + B_0^4 O_0^4 + B_0^6 O_0^6 + B_6^6 O_6^6 + B_4^3 O_4^3 + B_6^3 O_6^3 \tag{28}$$

respectively. Where the B_l^q are the crystal field parameters, which can in principle be calculated if the charge distribution is known, and the O_l^q are Stevens operators. The effect of these operators on the J=8 manifold can be seen by expanding the operators as polynomials of the $\hat{J}$, $\hat{J}_z$ and $\hat{J}_\pm$ operators. Stevens operators in the form O_0^q form the diagonal of $V_{\rm CF}$ and only depend on $\hat{J}$ and $\hat{J}_z$. Therefore they do not couple states with differing m_z. Operators in the form O_l^q form the off-diagonal components of $V_{\rm CF}$ and contain terms with $\hat{J}_\pm$, thereby coupling terms with m_z that differ by $\pm q$.

Thus, one can immediately see the effect of the crystal field from the form of the potentials written above. For the C_{3v} symmetric crystal field, states with $|m_z\rangle$ differing by either $|\pm 3\rangle$ or $|\pm 6\rangle$ are coupled. The result is a spectrum of singlets and doublets in the form:

$$|\psi\rangle = a\,|6\rangle + b\,|3\rangle + c\,|0\rangle + d\,|-3\rangle + e\,|-6\rangle\,, \tag{29}$$

and

$$|\phi\rangle = a\,|\pm 8\rangle + b\,|\pm 5\rangle + c\,|\pm 2\rangle + d\,|\mp 1\rangle + e\,|\mp 4\rangle + f\,|\mp 7\rangle\,. \tag{30}$$

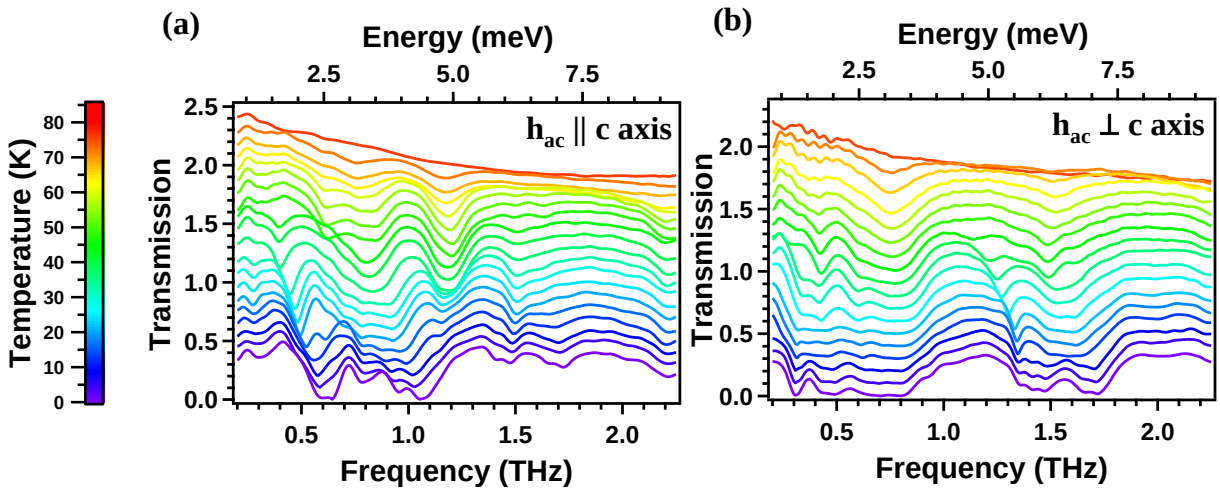

FIG. 10: (a)-(b) Magnitude of the complex transmission as a function of frequency and temperature for the (a) $\vec{\mathrm{h}}_{\mathrm{ac}} \parallel c$ and (b) $\vec{\mathrm{h}}_{\mathrm{ac}} \perp c$ geometries respectively. Curves are offset by 0.1 per temperature for clarity.

respectively. The case of C_3 crystal field is qualitatively similar. Here the reduction of symmetry results in coupling of states with $|m_z\rangle$ only differing by $|\pm 6\rangle$. The result is still a spectrum of singlets and doublets with the doublet states being identical to those of the C_{3v} crystal field listed above. However, the singlets can take the form of either:

$$|\phi\rangle = a\,|6\rangle + b\,|0\rangle + c\,|-6\rangle\,, \tag{31}$$

or

$$|\phi\rangle = \frac{1}{\sqrt{2}}(|3\rangle \pm |-3\rangle), \tag{32}$$

respectively.

The above calculation predicts a spectrum of singlets and doublets but the ordering of the energy levels depends on the prefactors (a, b, c,...) of the states listed above which are difficult to calculate. Instead, the ordering of the spectrum is determined experimentally by probing degeneracies via Zeeman interaction under applied field as well as the optical selection rules of the system. With the quantization axis along the hexagonal c direction, one expects that for h$\perp$c polarization to couple states with $\Delta \mathrm{m}_z = \pm 1$. Thereby allowing transitions between singlets and doublets or between different doublets. With h$\|$c, one expects transitions with $\Delta \mathrm{m}_z = 0$ i.e. within doublets.

However, additional effects which depart from the simplistic picture of only spin-orbit coupling and crystal field splitting outlined above must also be considered. For instance, the Ho sites of the crystal lattice lack inversion symmetry which permits electric dipole excitations, the selection rules of which depend on the detailed form of the crystal field. Additionally, Ho electrons can also interact with the nuclear spin of Ho^{+3} ion thereby introducing hyperfine magnetic dipole and electric quadrupole terms into the Hamiltonian. Magnetic exchange represents an additional energys scale which will further modify the crystal field spectrum. All such effects will work in tandem to produce the crystal field spectrum observed in HMO. It should noted that the J=8 Ho^{+3} ions are non-Kramers ions and thus any degeneracy is not protected by symmetry. Therefore, one may generally expect a crystal field spectrum which is considerably more complex than one of temperature independent singlets and doublets.

Temperature Dependence Of The Crystal Field Spectra

While image plots of the full temperature dependence of HMO can be seen in Figure 1 of the main text, we neglected to discuss the finer details of the crystal field spectrum. Here we display the full temperature dependent data set as well as describe the crystal field spectra of HMO in more detail. Figure 10 displays the magnitude of the complex transmission, the "raw" data from our TDTS measurements, as a function of frequency and temperature for measurement geometries (a) $\vec{\mathrm{h}}_{\mathrm{ac}} \parallel c$ and (b) $\vec{\mathrm{h}}_{\mathrm{ac}} \perp c$ respectively. One can show that the axial symmetry of the lattice constrains the transmission matrix such that only these two orientations give unique responses in zero field. Curves

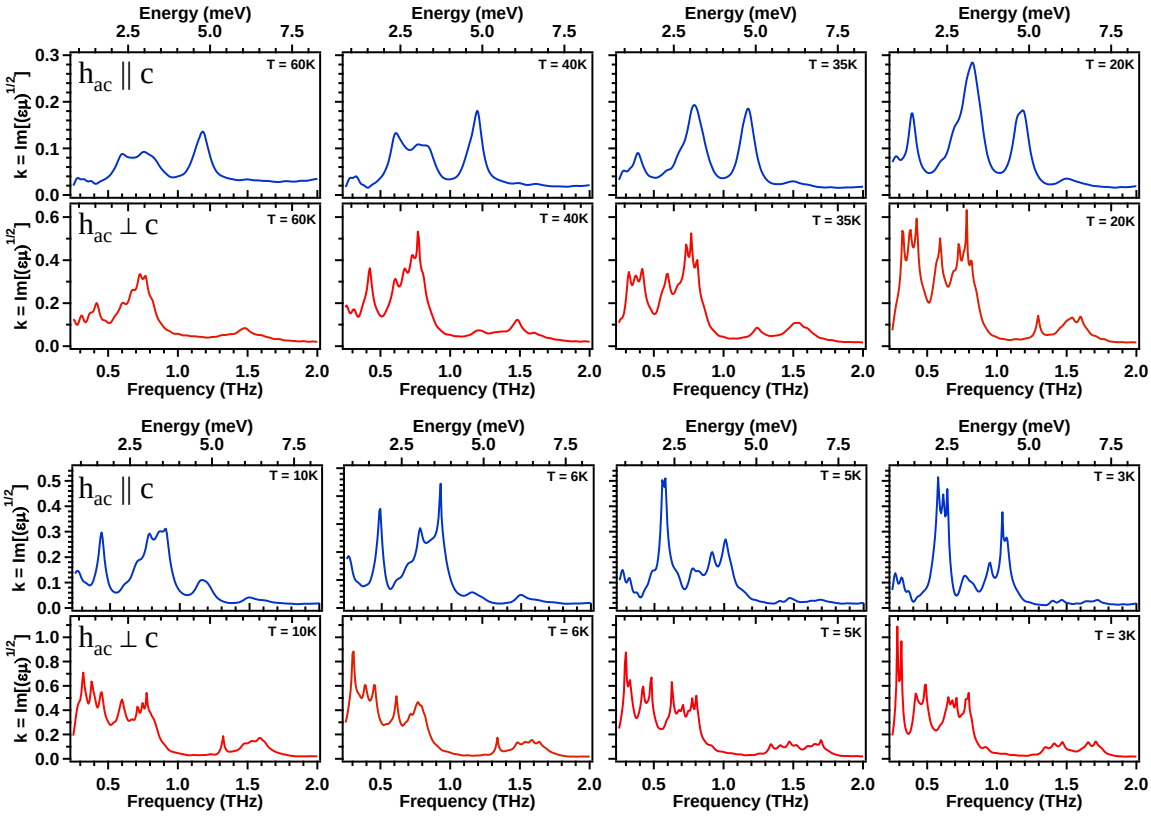

FIG. 11: The dissipative part of the index of refraction, $k = \mathbb{I}\mathrm{m}\{\sqrt{\epsilon\mu}\}$, for the $\vec{h}_{ac} \parallel c$ (top rows, blue) and $\vec{h}_{ac} \perp c$ orientations (bottom rows, red) at several representative temperatures. Absorptions in the transmission are dissipative and therefore correspond to peaks in k. Dramatic changes in the spectra are observed across the zero field transitions $T_{SR} \approx 37$ K and $T_{Ho} \approx 5.25$K.

are offset by 0.1 per temperature for clarity. The complex transmissions were then numerically inverted to extract the complex index of refraction of the sample. Figure 11 displays the extracted imaginary part of the index of refraction for both zero field orientations at several representative temperatures. These are the data that were used to generate the image plots shown in Figure 1 of the main text. One can see that the spectra is dominated by strong dissipation due to Ho ($^5I_8$) crystal field excitations below 1 THz and around 1.5 THz. The excitation at 1.3 THz in the $\vec{h}_{ac} \perp c$ orientation is the Mn AFR.

One can see from Figure 11 that the crystal field spectra becomes considerably complex as the temperature is reduced, strongly departing from the simplistic picture of singlets and doublets outlined above. Many crystal field excitations split into clusters of closely packed and highly overlapping excitations at low temperatures. In order to better understand the crystal field spectrum, the imaginary part of the index of refraction were fit to a generic model of Lorentzian oscillators on a linear background. Here our analysis will be restricted to only the crystal field excitation energies as their intensities and widths are difficult to extract with so many overlapping excitations.

Figure 12 displays the excitation energies as a function of temperature for both measurement geometries obtained from fitting the spectra. Vertical dashed lines mark the three zero field transition temperatures T_N, T_{SR}, and T_{Ho}. Color denotes distinct crystal field excitations many of which split into a multiplet of nearly degenerate excitations as the temperature is reduced. Although new excitations develop at both T_{SR} and T_{Ho}, the energy spectrum shown in Figure 12 shows relatively weak temperature dependence above T_{Ho}. This is consistent with optical spectroscopy of other hexagonal manganites [27] and the related compound $HoMn_2O_5$ [45] which observe that the energy eigenvalues of the crystal field spectrum to be nearly independent of magnetic ordering, even in manganites possessing rare earth magnetism. Instead, magnetic exchange manifests itself was a redistribution of spectral weight between optically active excitations. This has previously been explained as stemming from the change in symmetry of the ligand field at the rare-earth site as new magnetic order develops. The crystal field, being the dominant term in the Hamiltonian, sets the energies of the excitation spectrum while the weaker exchange term modifies the selection rules of the system in such a way to respect the change in symmetry that accompanies magnetic order. The modified selection rules then

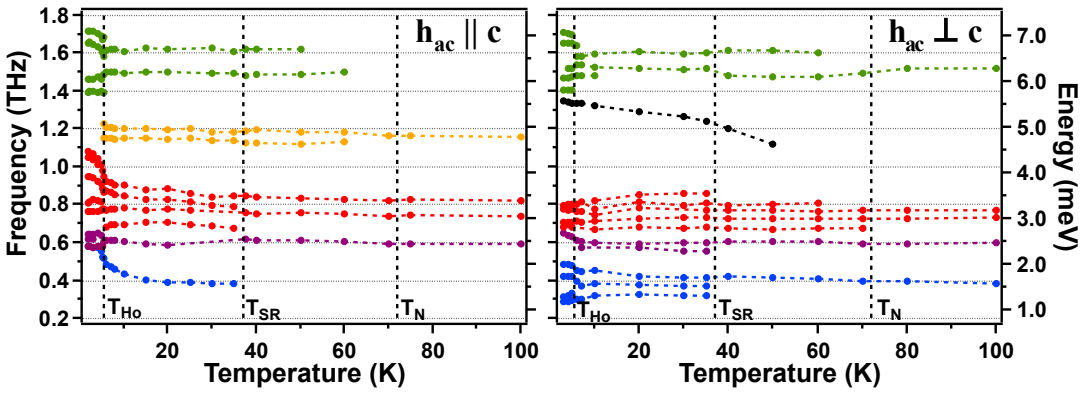

FIG. 12: Temperature dependence of the infrared excitation energies of HMO derived from fitting the imaginary part of the index of refraction for the (left) $\vec{h}_{ac} \parallel c$ and (right) $\vec{h}_{ac} \perp c$ orientations. Color denotes each family of excitations. The black curve in the $\vec{h}_{ac} \perp c$ orientation is the Mn AFR. Vertical dashed lines mark the three transition temperatures T_N, T_{SR}, and T_{Ho}.

shift spectral weight between excitations.

However, unlike the transitions at T_N and T_{SR}, the spectra at T_{Ho} displays a dramatic renormalization of the crystal field excitation energies. This low temperature energy renormalization, which has not been previously identified, presumably stems from magnetic exchange interactions in HMO. Whether such exchange is between Ho-Ho or Ho-Mn moments remains an open question. However, Ho-Mn interactions are expected to be roughly an order of magnitude stronger than Ho-Ho exchange and as we demonstrated in the main text, Ho-Mn interactions are particularly strong in HMO. Therefore, we speculate that such a renormalization of the Ho crystal field spectrum below T_{Ho} may stem from Ho-Mn exchange but further investigation is required to confirm.

Excitation	Energy ($T > T_{SR}$)	Previously Reported Energies	Optically Active $h_{ac} \parallel c$	Optically Active $h_{ac} \perp c$
CF 1	1.51 meV	1.48 meV (Ref. [21])	$T_{Ho} < T < T_{SR}$	Always Active
CF 2	2.43 meV	2.41 meV (Ref. [21])	$T > T_{SR}$ $T < T_{Ho}$	Always Active
CF 3	3.09 meV & 3.40 meV	3.13 meV (Ref. [21]) 3.40 meV (Ref. [6])	Always Active	Always Active
CF 4	4.68 meV & 4.89 meV	4.84 meV (Ref. [6])	$T > T_{Ho}$	Never Active
CF 5	6.17 meV & 6.71 meV	6.46 meV (Ref. [6])	Always Active	Always Active

TABLE I: Summary of our characterization of the crystal field spectra of HMO. Crystal field excitation energies are reported at temperatures $T > T_{SR}$. Also included are previously reported crystal field energies found via neutron scattering [21] and infrared spectroscopy [6]. Values from Ref. 6 were reported at T = 10K. CF 4 was observed in Ref. 6 but it's energy was not reported. The value listed in the table is estimated from figure 1 of Ref. 6. Several crystal field excitations are reported here for the first time.

Table I summarizes our characterization of the low energy excitation spectrum of HMO. Excitation energies, reported for temperatures $T > T_{SR}$, are shown as well as a comparison to previously reported values, although several excitations are reported here for the first time. Additonally shown are the selection rules by measurement orientation for each excitation.

FULL MAGNETIC FIELD DEPENDENCE

In the main text, data was shown only in the orientation in which the THz oscillatory magnetic field $\vec{h}_{ac} \perp c$ and the applied dc magnetic field $\vec{H}_{dc} \parallel c$ and only at 20 K. In this section, we display the full data set for this orientation as well as other orientations obtained by varying the direction of $\vec{h}_{ac}$ and $\vec{H}_{dc}$ with respect to the c axis.

$\vec{\mathbf{h}}_{\mathbf{ac}} \perp \mathbf{c}, \vec{\mathbf{H}}_{\mathbf{dc}} \parallel \mathbf{c}$

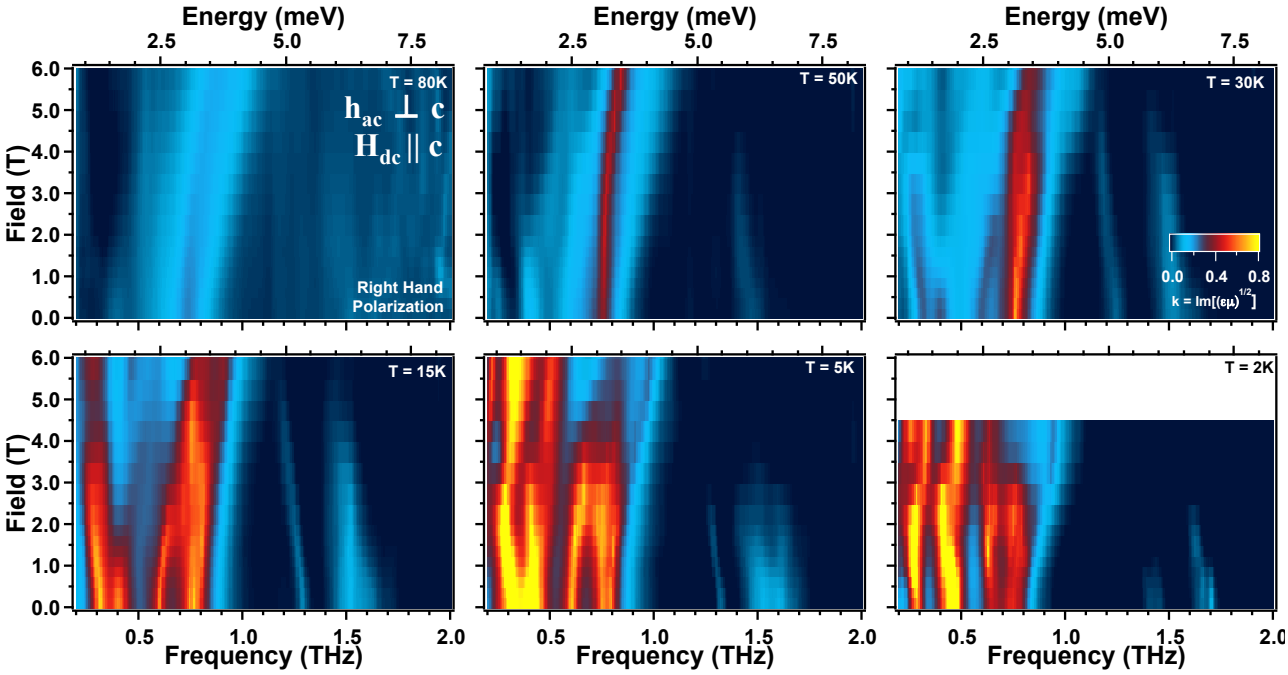

FIG. 13: Image plots of the imaginary part of the index of refraction with the THz oscillatory magnetic field $\vec{\mathrm{h}}_{\mathrm{ac}} \perp \mathrm{c}$ and the applied dc magnetic field $\vec{\mathrm{H}}_{\mathrm{dc}} \parallel \mathrm{c}$ at several representative temperatures. Data is presented in the in the right hand channel of the circular basis.

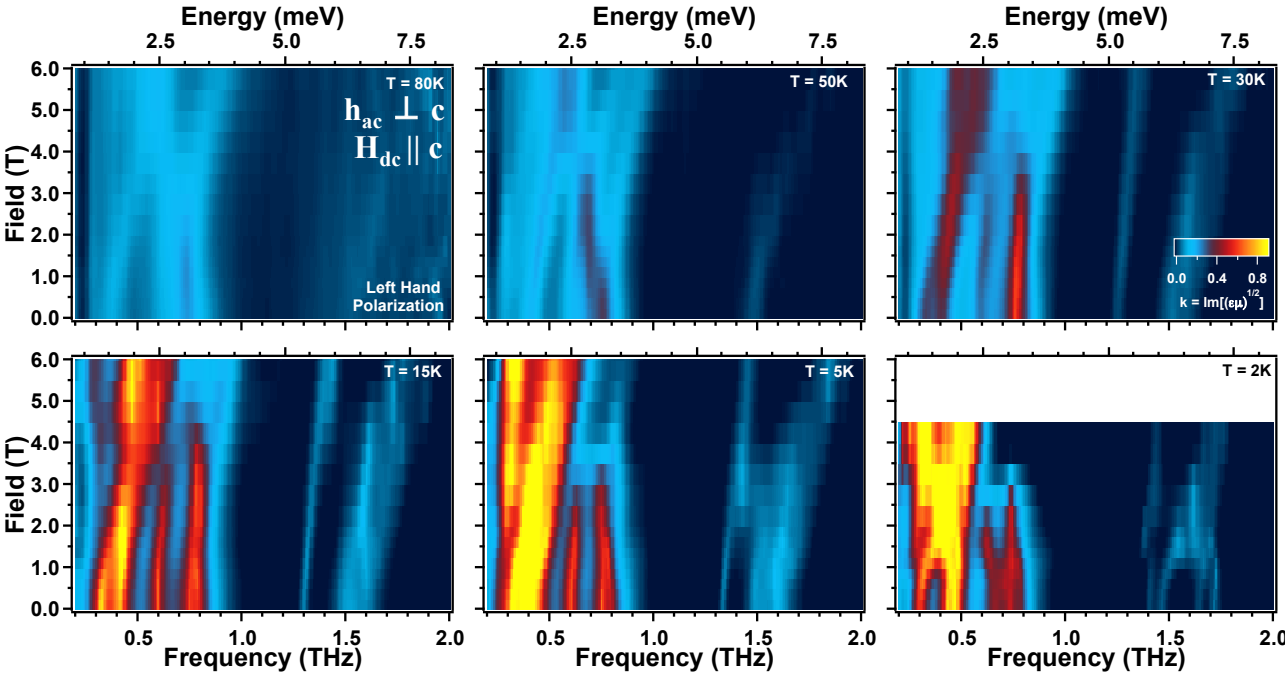

FIG. 14: Image plots of the imaginary part of the index of refraction with the THz oscillatory magnetic field $\vec{\mathrm{h}}_{\mathrm{ac}} \perp \mathrm{c}$ and the applied dc magnetic field $\vec{\mathrm{H}}_{\mathrm{dc}} \parallel \mathrm{c}$ at several representative temperatures. Data is presented in the in the left hand channel of the circular basis.

$\vec{\mathbf{h}}_{\mathbf{ac}} \parallel \mathbf{c}, \vec{\mathbf{H}}_{\mathbf{dc}} \perp \mathbf{c}$

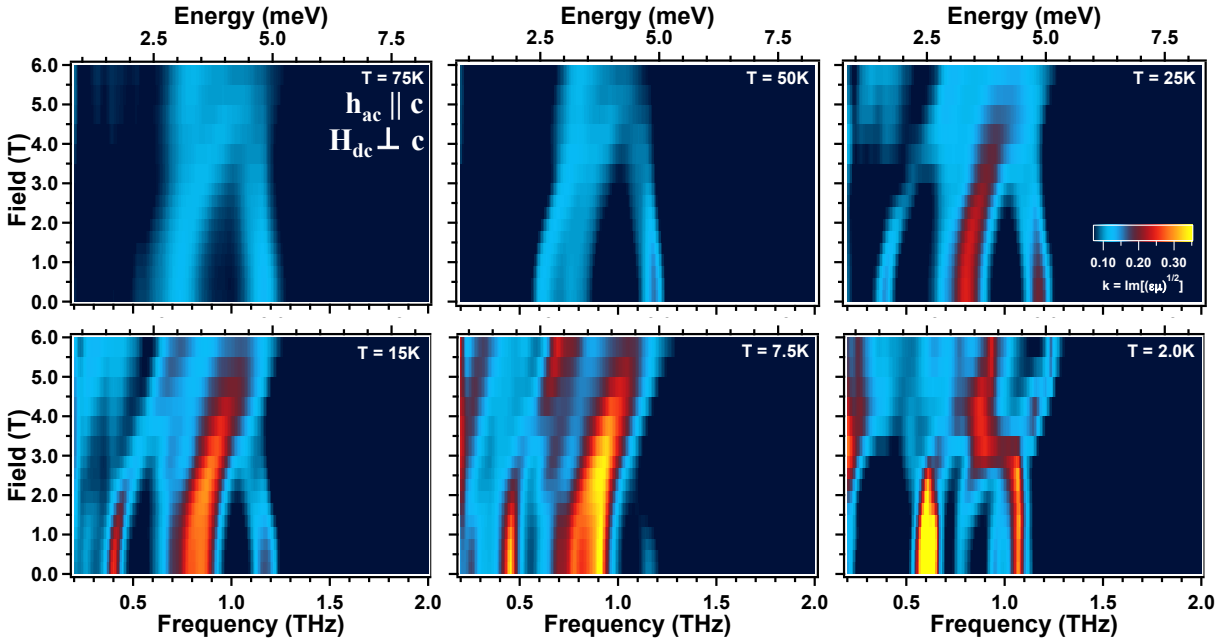

FIG. 15: Image plots of the imaginary part of the index of refraction with the THz oscillatory magnetic field $\vec{\mathrm{h}}_{\mathrm{ac}} \parallel \mathrm{c}$ and the applied dc magnetic field $\vec{\mathrm{H}}_{\mathrm{dc}} \perp \mathrm{c}$ at several representative temperatures.

$\vec{\mathbf{h}}_{\mathbf{ac}} \perp \mathbf{c}, \vec{\mathbf{H}}_{\mathbf{dc}} \perp \mathbf{c}$

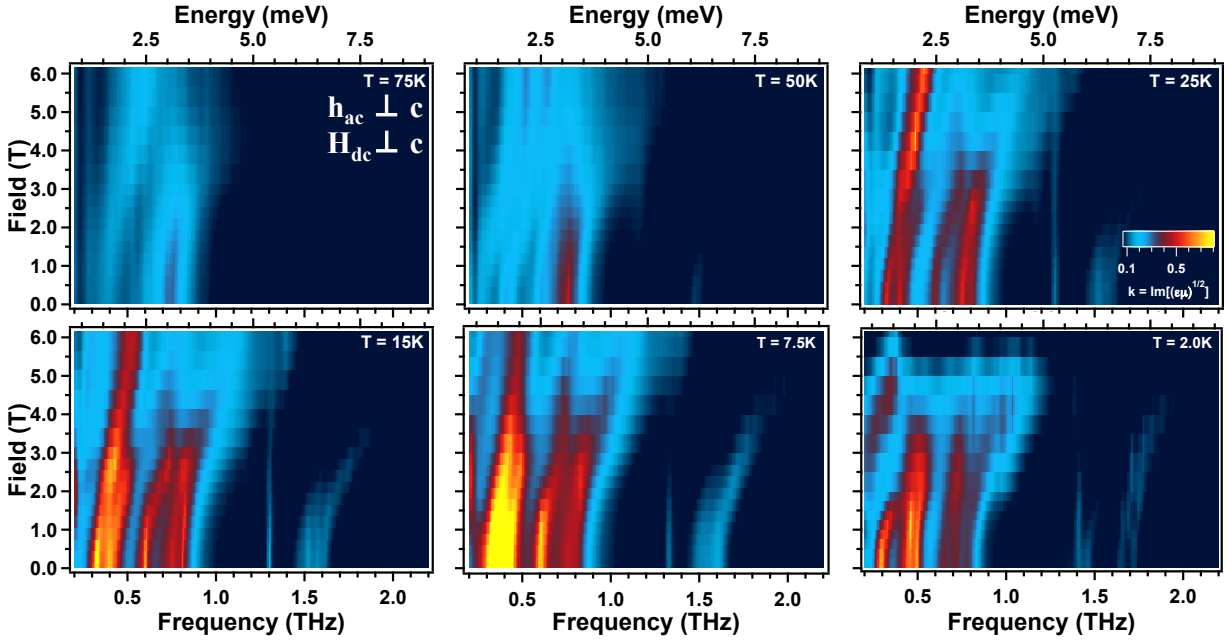

FIG. 16: Image plots of the imaginary part of the index of refraction with the THz oscillatory magnetic field $\vec{\mathrm{h}}_{\mathrm{ac}} \perp \mathrm{c}$ and the applied dc magnetic field $\vec{\mathrm{H}}_{\mathrm{dc}} \perp \mathrm{c}$ at several representative temperatures.

[1] B. Lorenz, ISRN Condensed Matter Physics **vol. 2013** (2013).
[2] N. Hur, I. K. Jeong, M. F. Hundley, S. B. Kim, and S.-W. Cheong, Phys. Rev. B **79**, 134120 (2009).
[3] S. Nandi, A. Kreyssig, L. Tan, J. W. Kim, J. Q. Yan, J. C. Lang, D. Haskel, R. J. McQueeney, and A. I. Goldman, Phys. Rev. Lett. **100**, 217201 (2008).
[4] M. Fiebig, C. Degenhardt, and R. V. Pisarev, Phys. Rev. Lett. **88**, 027203 (2001).
[5] X. Fabrèges, I. Mirebeau, P. Bonville, S. Petit, G. Lebras-Jasmin, A. Forget, G. André, and S. Pailhès, Phys. Rev. B **78**, 214422 (2008).
[6] D. Talbayev, A. D. LaForge, S. A. Trugman, N. Hur, A. J. Taylor, R. D. Averitt, and D. N. Basov, Phys. Rev. Lett. **101**, 247601 (2008).
[7] D. Meier, H. Ryll, K. Kiefer, B. Klemke, J.-U. Hoffmann, R. Ramesh, and M. Fiebig, Phys. Rev. B **86**, 184415 (2012).
[8] S. G. Condran and M. L. Plumer, Journal of Physics: Condensed Matter **22**, 162201 (2010).
[9] T. Lottermoser, T. Lonkai, U. Amann, D. Holhwein, J. Ihringer, and M. Fiebig, Nature **430**, 541 (2003).
[10] B. G. Ueland, J. W. Lynn, M. Laver, Y. J. Choi, and S.-W. Cheong, Phys. Rev. Lett. **104**, 147204 (2010).
[11] B. Lorenz, A. P. Litvinchuk, M. M. Gospodinov, and C. W. Chu, Phys. Rev. Lett. **92**, 087204 (2004).
[12] C. dela Cruz, F. Yen, B. Lorenz, Y. Q. Wang, Y. Y. Sun, M. M. Gospodinov, and C. W. Chu, Phys. Rev. B **71**, 060407 (2005).
[13] N. Iwata and K. Kohn, Journal of the Physical Society of Japan **67**, 3318 (1998).
[14] F. Yen, C. R. dela Cruz, B. Lorenz, Y. Y. Sun, Y. Q. Wang, M. M. Gospodinov, and C. W. Chu, Phys. Rev. B **71**, 180407 (2005).
[15] S.-W. Cheong and M. Mostovoy, Nat. Mater. **6**, 13 (2007).
[16] B. B. Van Aken, T. T. M. Palstra, A. Filippetti, and A. Nicola, Nat. Mater. **3**, 164 (2004).
[17] C. J. Fennie and K. M. Rabe, Phys. Rev. B **72**, 100103 (2005).
[18] M. Fiebig, D. Fröhlich, K. Kohn, S. Leute, T. Lottermoser, V. V. Pavlov, and R. V. Pisarev, Phys. Rev. Lett. **84**, 5620 (2000).
[19] M. Fiebig, C. Degenhardt, and R. V. Pisarev, Journal of Applied Physics **91**, 8867 (2002).
[20] M. Fiebig, T. Lottermoser, and R. V. Pisarev, Journal of Applied Physics **93**, 8194 (2003).
[21] O. P. Vajk, M. Kenzelmann, J. W. Lynn, S. B. Kim, and S.-W. Cheong, Phys. Rev. Lett. **94**, 087601 (2005).
[22] P. J. Brown and T. Chatterji, Journal of Physics: Condensed Matter **18**, 10085 (2006).
[23] P. J. Brown and T. Chatterji, Phys. Rev. B **77**, 104407 (2008).
[24] H. Sugie, N. Iwata, and K. Kohn, Journal of the Physical Society of Japan **71**, 1558 (2002).
[25] T. Lonkai, D. Hohlwein, J. Ihringer, and W. Prandl, Applied Physics A **74** (2002).
[26] W. Palme, F. Mertens, O. Born, and B. L uthi, Solid State Commun. **76**, 873 (1990).
[27] E. C. Standard, T. Stanislavchuk, A. A. Sirenko, N. Lee, and S.-W. Cheong, Phys. Rev. B **85**, 144422 (2012).
[28] I. Dzyaloshinsky, Journal of Physics and Chemistry of Solids **4**, 241 (1958).
[29] T. Moriya, Phys. Rev. **120**, 91 (1960).
[30] N. J. Laurita, B. Cheng, R. Barkhouser, V. A. Neumann, and N. P. Armitage, Journal of Infrared, Millimeter, and Terahertz Waves pp. 1–9 (2016).
[31] N. P. Armitage, Phys. Rev. B **90**, 035135 (2014).
[32] C. M. Morris, R. V. Aguilar, A. V. Stier, and N. P. Armitage, Opt. Express **20**, 12303 (2012).
[33] B. R. Judd, Proceedings of the Royal Society of London A: Mathematical, Physical and Engineering Sciences **232**, 458 (1955).
[34] A. Abragam and B. Bleaney, *Electron Paramagnetic Resonance* (Clarendon Press, Oxford, 1970).
[35] R. J. Elliott and K. W. H. Stevens, Proceedings of the Royal Society of London A: Mathematical, Physical and Engineering Sciences **218**, 553 (1953).
[36] S. Rosenkranz, A. P. Ramirez, A. Hayashi, R. J. Cava, R. Siddharthan, and B. S. Shastry, Journal of Applied Physics **87**, 5914 (2000).
[37] U. Ranon and K. Lee, Phys. Rev. **188**, 539 (1969).
[38] See Supplemental Information.
[39] K. Momma and F. Izumi, Journal of Applied Crystallography **44**, 1272 (2011).
[40] P. Coeure and *et al.*, Proc. of 1st Intl. Meeting on Ferroelectricity (Institute of Physics, Czech. Acad. Sci., Prague), p. 332 (1966).
[41] R. C. Jones, J. Opt. Soc. Am. **31**, 488 (1941).
[42] A. Altland and B. D. Simons, *Condensed Matter Field Theory* (Cambridge University Press, New York, 2010), 2nd ed., ISBN 978-0521769754.
[43] S. G. Condran and M. L. Plumer, J. Phys.: Condens. Matter **22**, 162201 (2010).
[44] K. Stevens, Physics Letters A **47**, 401 (1974), ISSN 0375-9601.
[45] A. A. Sirenko, S. M. O'Malley, K. H. Ahn, S. Park, G. L. Carr, and S.-W. Cheong, Phys. Rev. B **78**, 174405 (2008).